Inorganic Chemistry

pubs.acs.org/IC

Article

Necrosis-Inducing High-Valent Oxo−Rhenium(V) Complexes with Potent Antitumor Activity: Synthesis, Aquation Chemistry, Cisplatin Cross-Resistance Profile, and Mechanism of Action

Shubhangi Das, Pulkit Joshi, and Malay Patra*

Cite This: *Inorg. Chem.* 2023, 62, 19720−19733

Read Online

ACCESS | Metrics & More | Article Recommendations | Supporting Information

ABSTRACT: Chemotherapy with the cytotoxic platinum (Pt) drugs cisplatin, carboplatin, and oxaliplatin is the mainstay of anticancer therapy in the clinic. The antitumor activity of Pt drugs originates from their ability to induce apoptosis via covalent adduct formation with nuclear DNA. While the phenomenal clinical success is highly encouraging, resistance and adverse toxic side effects limit the wider applicability of Pt drugs. To circumvent these limitations, we embarked on an effort to explore the antitumor potential of a new class of oxo−rhenium(V) complexes of the type [(N^N)(EG)Re(O)Cl] (where EG = ethylene glycolate and N^N = bipyridine, Bpy (**1**); phenanthroline, Phen (**2**); 3,4,7,8-tetramethylphenanthroline, Me_4Phen (**3**)). Investigation of speciation chemistry in aqueous media revealed the formation of [(N^N)Re(O)$(OH)_3$] as the biologically active species. Complex **3** was found to be the most potent among the three, with IC_{50} values ranging from 0.1 to 0.4 μM against a panel of cancer cells, which is 5−70-fold lower when compared with cisplatin. The higher potency of **3** is attributed to its higher lipophilicity, which enhanced cellular uptake. Importantly, complex **3** efficiently overcomes cisplatin resistance in ovarian, lung, and prostate cancer cells. In addition to reporting the aquation chemistry and identifying the active species in aqueous media, we performed in-depth in vitro mechanistic studies, which revealed that complex **3** preferentially accumulates in mitochondria, depletes mitochondrial membrane potential, and upregulates intracellular reactive oxygen species (ROS), leading to ER stress-mediated necrosis-mediated cancer cell death.

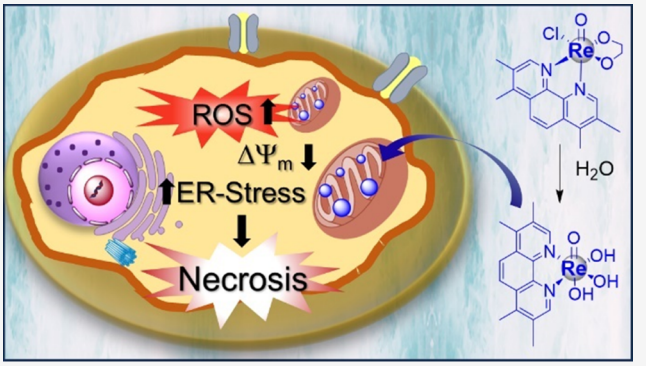

INTRODUCTION

Cancer is the second leading cause of death after cardiovascular diseases, accounting for 10 million deaths and 20 million new cases in 2020.[1] Even in the modern era of personalized therapy and immunotherapy, chemotherapy with platinum (Pt) drugs—cisplatin, carboplatin, and oxaliplatin remains the mainstay of cancer management in the clinic.[2−4] In fact, approximately half of all patients receiving chemotherapy are being treated with Pt drugs either as a single agent or in combination with other drugs or treatment modalities.[3,5] However, in spite of this remarkable clinical success, Pt drugs suffer from two critical limitations.[4] Innate and acquired resistance against Pt drugs increasingly reduce their efficacy, leading to treatment failure.[6] Further, severe side effects, such as nephrotoxicity, neurotoxicity, myelosuppression, etc., arising from the indiscriminate killing of cancer and normal cells, limit their applicability as well as dose escalation during the treatment cycle.[4,7] To overcome these limitations, tremendous efforts have been devoted toward the development of non-Pt metal-based drugs with a mechanism of action different from the DNA-targeted Pt drugs, and promising results were obtained using ruthenium (Ru), gold (Au), iridium (Ir), and rhenium (Re) complexes.[8−12]

In the past decade, Re(I) complexes of the type [(N^N)$Re(CO)_3X$] (N^N = polypyridyl ligands and X = Cl, H_2O, isonitriles, pyridyl, phosphines, etc.) have emerged as a promising class of antitumor agents.[13,14] Wilson et al. developed several highly in vitro as well as in vivo potent Re(I) complexes.[15−19] Notably, this class of complexes are endowed with the extraordinary ability of overcoming cisplatin resistance in cervical, ovarian, and lung cancer cells, owing to their novel mechanism of action.[15] Zobi and co-workers recently demonstrated potent antiangiogenic and antimetastatic properties of the $Re(CO)_3$ systems.[20,21] Massi and Falasca et al. introduced $Re(CO)_3$ complexes bearing *N*-

Received: September 6, 2023
Revised: November 2, 2023
Accepted: November 2, 2023
Published: November 16, 2023

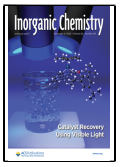

https://doi.org/10.1021/acs.inorgchem.3c03110
Inorg. Chem. 2023, 62, 19720−19733

heterocyclic carbene ligands, which exerted antitumor activity via inhibiting important cell signaling processes.[22,23]

Additionally, the rich spectroscopic properties of Re(I) systems offer numerous unique advantages over the classical Pt drugs. For instance, the luminescent properties and distinct Re−C≡O stretching enable real-time intracellular tracking of Re(I) complexes via fluorescence and vibrational microscopies, which facilitates mechanistic investigation.[24,25] Further, the possibility of synthesizing the "hot" ^{99m}Tc analogue provides the opportunity for pharmacokinetic assessment through in vivo imaging in the very early developmental stage of Re(I) antitumor agents.[15]

By contrast to the Re(I) system, the antitumor potential of high-valent Re complexes was poorly explored. Investigations on the antitumor properties of Re(III) clusters by Schtemenko et al. led to the identification of paddle wheel dirrhenate(III) complexes with remarkable in vivo anticancer properties and low neuro-, nephro- and hepato-toxicities.[26−28] An octahedral Re(IV) complex was also shown to display potent in vitro antitumor activity against breast, ovarian, and prostate cancer cells.[29] The antitumor activity of Re(V)=O systems was first demonstrated in 2013 by Abram et al. using an in vitro screening of a few Re(V)=O complexes containing S,N,S-tridentate thiosemicarbazone/thiosemicarbazide ligands.[30] Their best candidate **Re-1** (Figure 1 for the structure) exerted

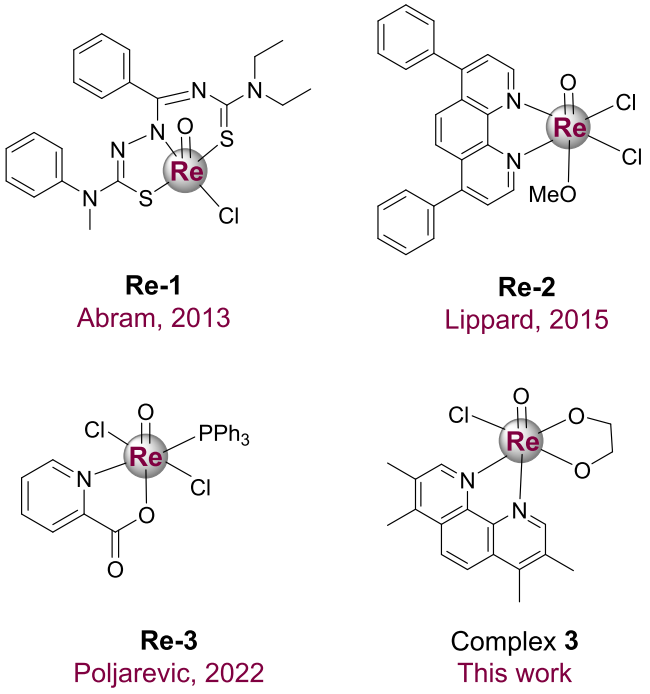

Figure 1. Structures of Re(V)=O complexes investigated previously and in this work.

an IC_{50} value (half inhibitory concentration) of 0.41 μM against MCF-7 breast cancer cells. Soon after that, remarkably in vitro potent Re(V)=O complexes of phenanthroline-based ligands, such as **Re-2** (Figure 1 for the structure), were reported by Lippard and co-workers.[31] Importantly, in addition to potent activity against cisplatin-sensitive and -resistant cells with IC_{50} vales 0.04−8.6 μM, **Re-2** was shown to promote necroptosis-mediated cancer cell death via oxidative stress induction. Further, **Re-2** possessed remarkable in vivo tolerability in C57BL/6 mice. In a recent paper by Poljarević et al., in vitro antitumor activity of phosphine-containing Re(V)=O complexes, such as **Re-3** (Figure 1 for the structure), in combination with verapamil hydrochloride and L-buthionine-sulfoximine was investigated.[32] However, this class of complexes presented poor in vitro potency with IC_{50} > 50 μM. Besides the antitumor research, the thiophilic nature of Re(V)=O complexes was exploited for the development of covalent inhibitors of thiol-containing enzymes, such as cystine proteases and cathepsins.[33−36]

These aforementioned fascinating properties of Re(V)=O complexes intrigued us to investigate the antitumor properties of a new class of such complexes consisting of N^N and O^O bidentate ligands (Figure 1). Herein, we report synthesis, characterization, aquation chemistry, and biological evaluation of Re(V)=O complexes with general formula [(N^N)(EG)-Re(O)Cl] (where EG = ethylene glycolate and N^N = bipyridine, Bpy (**1**); phenanthroline, Phen (**2**); 3,4,7,8-tetramethyl-phenanthroline, Me_4Phen (**3**)). While the O^O and Cl ligands were kept unchanged in all complexes, the N^N ligand was varied to tune the lipophilicity of this class of Re(V)=O complexes. It is worth noting that the EG ligand was chosen due to its proven ability to strongly coordinate with the Re(V)=O and Te(V)=O cores and form stable complexes for medicinal and radiopharmaceutical applications.[37,38] We showed that the most potent candidate complex **3** possesses outstanding antitumor activity over a panel of cancer cells and has the ability to overcome cisplatin resistance in ovarian, lung, and prostate cancer cells. The potency of **3** was found to be comparable to or slightly higher than that of the previously reported most potent compound **Re-2**. In addition to reporting the aquation chemistry of these Re(V)=O complexes and identifying the active species in biological media for the first time, we performed in-depth mechanistic studies, which revealed that complex **3** preferentially accumulates in mitochondria, depletes mitochondrial membrane potential, and upregulates intracellular ROS, leading to ER stress-mediated necrosis-mediated cancer cell death.

RESULTS AND DISCUSSION

Synthesis, Characterization, and Theoretical Studies. The synthesis of Re(V)=O complexes **1**−**3** is presented in Scheme 1a, and details are provided in the Experimental Section.[38] Briefly, a solution of $[(Bu)_4N][ReOCl_4]$ in methanol was treated with ethylene glycol (H_2EG). To this, addition of N^N bidentate ligands Bpy, Phen, and Me_4Phen afforded **1**, **2**, and **3**, respectively, as a reddish brown solid. All complexes were fully characterized using ^{1}H and ^{13}C NMR spectroscopies and matrix-assisted laser desorption/ionization-time-of-flight (MALDI-TOF) mass spectrometry (Figures S1−S9). The ^{1}H and ^{13}C NMR spectra of the complexes indicated that both polypyridyl N^N and EG ligands are coordinated to the Re(V)=O center. For instance, while the ^{1}H NMR spectrum of free Me_4Phen showed two sets of signals for four aromatic C−*H* protons owing to the presence of symmetry, the ^{1}H NMR spectrum of complex **3** showed four peaks due to the loss of symmetry upon coordination. Additionally, the EG ligand protons in complex **3** appeared as four significantly downfield-shifted signals as compared to the single peak observed for the free H_2EG. Purities of **1**−**3** were confirmed to be >95% by elemental microanalysis.

In principle, the ligands in a complex of the [(N^N)(O^O)-Re(O)Cl] type may adopt three different orientations, resulting in two unsymmetric isomers **A** and **B** (which may

https://doi.org/10.1021/acs.inorgchem.3c03110
Inorg. Chem. 2023, 62, 19720−19733

Scheme 1. (a) Synthesis of [(N^N)(EG)Re(O)Cl] Complexes 1−3. (b) Possible Ligand Orientations in [(N^N)(O^O)Re(O)Cl] Type Complexes

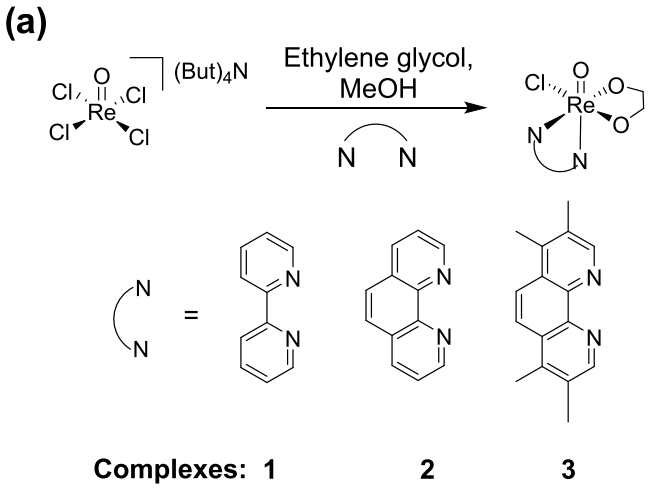

exist as a mixture of enantiomers) and one symmetric isomer **C** (Scheme 1b). ^{1}H and ^{13}C NMR spectra of **1**−**3** suggested the presence of a single unsymmetric species, either **A** or **B**, and the absence of symmetric isomer **C** (Figures S1, S2, S4, S5, S7, and S8). However, ^{1}H NMR cannot distinguish between two unsymmetrical isomers **A** and **B**. Unfortunately, despite repeated efforts, we were unsuccessful in growing good-quality single crystals of these complexes for the determination of their molecular structures, which prevented us from determining unambiguous ligand orientation around the Re(V) center.

In pursuit of this objective, we performed density functional theory (DFT) calculations using **3** as a representative of this class. Initially, we optimized the geometries in the gas phase, revealing that the **3B** isomer is energetically more stable than the **3A** isomer by approximately 16 kcal/mol (Figure 2a). Furthermore, we simulated the gas-phase ^{1}H NMR spectra of **3A** and **3B** and observed an overall better agreement for the **3B** isomer with the experimental spectrum than for **3A** (Figure 2b and Table S1). Particularly, the two of the glycolate protons are upfield shifted in the case of **3A** possibly due to the trans effect of the "=O" group, leading to only two peaks within the range of 4−6 ppm. Conversely, in the case of **3B**, all four glycolate protons are in good agreement with the experimental spectrum (Figure 2b). Taken together, the outcomes derived from the DFT calculations collectively lead us to formulate the hypothesis that the compound synthesized according to Scheme 1 likely assumes the isomeric configuration of **3B**. All of the computational details are provided later in the Experimental Section.

Aquation Chemistry and Stability in the Cell Culture Medium. With the complexes in hand, we first explored their aquation chemistry using ^{1}H NMR spectroscopy. Formation of an aqua complex (M−OH_2) through the exchange of the "Cl" ligand with water is considered an important activation step for anticancer metal complexes containing M−Cl bond(s).[4,11,12] A few previous reports also showed the hydrolysis of the Re−Cl bond in [(N^N)$(CO)_3$Re^{I}Cl] type anticancer complexes in aqueous media.[15,39] However, aquation chemistries of Re(V)=O anticancer complexes including **Re-1**, **Re-2**, and **Re-3** (Figure 1) remain unexplored. To initiate the study, complex **3** was dissolved in a mixture of DMSO-d_6 and D_2O (2:1, v/v), and the ^{1}H NMR spectrum was recorded at different time points. Results are presented in Figure 3a. DMSO, a routinely used solvent for preparation of a stock solution of drug candidates with poor water solubility, was used to ensure the

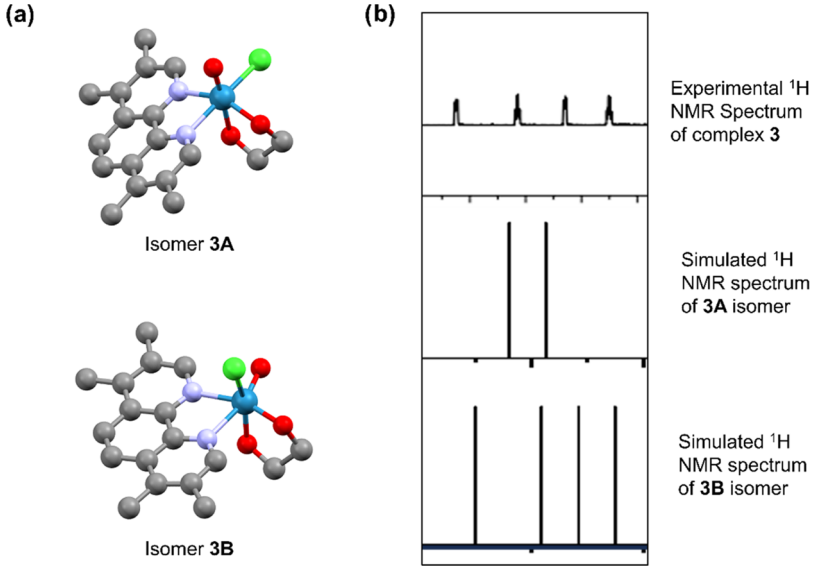

Figure 2. (a) DFT-optimized structures of **3A** and **3B** isomers. Color codes: cyan, Re; violet, N; red, O; green, Cl; gray, C. Hydrogen atoms are omitted for clarity. (b) Comparison of experimental ^{1}H NMR spectra of **3** (4−6 ppm, diastertopic CH_2 protons from the EG ligand) with simulated ^{1}H NMR spectra of isomers **3A** and **3B**. Full ^{1}H NMR spectra are presented in Figure S10.

https://doi.org/10.1021/acs.inorgchem.3c03110
Inorg. Chem. 2023, 62, 19720−19733

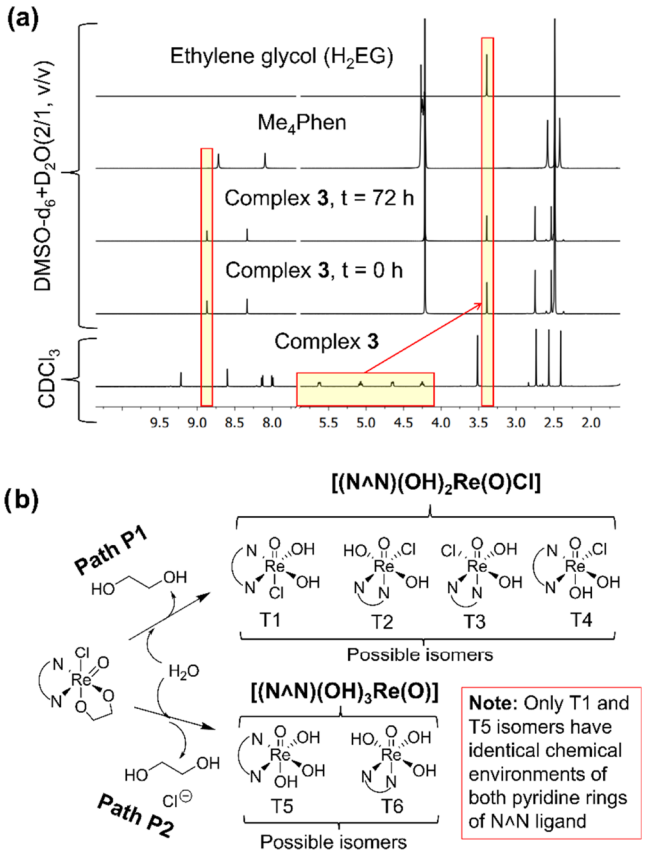

Figure 3. (a) Stacked ^{1}H NMR plot of complex **3** in the nonaqueous $CDCl_3$ medium and complex **3**, Me_4Phen, and ethylene glycol in aqueous media. (b) Two plausible and distinct hydrolysis pathways, P1 and P2, of [(N^N)(EG)Re(O)Cl] type complexes **1**–**3**. Hydrolysis via path P1 will result in the formation of [(N^N)-(OH)$_2$Re(O)Cl] that may exist as the T1, T2, T3, or T4 isomer. Hydrolysis via path P2 will result in the formation of [(N^N)-(OH)$_3$Re(O)] that may exist as T5 or T6 isomers. Note: Only T1 and T5 isomers, not T2, T3, T4, and T6, have identical chemical (or magnetic) environments for both the pyridine rings of the N^N ligands.

solubility of complex **3** in mM concentrations. Although we anticipated the hydrolysis of the Re(V)−Cl bond and formation of the corresponding hydrolyzed species, we were surprised to observe that unsymmetric complex **3** transformed to a single new symmetric species immediately after dissolving in aqueous media, as evidenced by the two pyridine rings of the N^N ligand showing identical chemical environments. The newly formed species remained unchanged over 72 h. While complex **3** presented four aromatic C*H* (8.0−9.2 ppm) and four aliphatic CH_3 (2.4−3.5 ppm) proton signals in non-aqueous solvents such as $CDCl_3$, the same complex showed two aromatic C*H* (8.3 and 8.9 ppm) and two aliphatic CH_3 (2.5 and 2.7 ppm) proton signals in the presence of D_2O (Figure 3a). Further, the four diasterotopic proton signals (4.2, 4.6, 5.1, and 5.6 ppm) from the EG ligand in **3** disappeared in aqueous media with the appearance of a new upfield shifted singlet at 3.4 ppm (Figure 3a). This new singlet was assigned to be the uncoordinated H_2EG by comparing it with the ^{1}H NMR spectrum of an authentic sample of H_2EG, indicating the release of the EG ligand from complex **3** in the presence of water. However, the Me_4Phen ligand remained attached to the Re(V)═O core in aqueous media, as evident from different ^{1}H NMR spectra of **3** and the free Me_4Phen ligand in aqueous media (Figure 3a). Although the ^{1}H NMR data confirmed the release of the EG ligand from complex **3**, it could not be ascertained from ^{1}H NMR spectroscopy whether the "Cl" ligand remains bound to the Re(V)═O core or replaced by water in the hydrolyzed species. To investigate this, we hypothesized that complex **3** may undergo hydrolysis via either the P1 or P2 pathway (Figure 3b). While the P1 pathway will lead to the formation of [(Me_4Phen)(OH)$_2$Re(O)Cl] through replacement of only the EG ligand by water, the P2 pathway will lead to the formation of [(Me_4Phen)(OH)$_3$Re(O)] through replacement of both EG and Cl ligands by water. As shown in Figure 3b, [(Me_4Phen)(OH)$_2$Re(O)Cl] can exist as four possible isomers in solution: T1, T2, T3, and T4. Similarly, [(Me_4Phen)(OH)$_3$Re(O)] can exist as two possible isomers, T5 and T6 (Figure 3b). Based on ^{1}H NMR data, the possibility of the existence of T2, T3, T4, and T6 isomers, where the two pyridine rings of the Me_4Phen N^N ligand have different chemical environments, can be ruled out. Then, we analyzed the key structural difference between the remaining two isomers, T1 and T5, where both pyridine rings of the Me_4Phen ligand have similar chemical environments (Figure 3b). While the labile "Cl" ligand is oriented *trans* to the "═O" ligand in T1, T5 does not contain any labile "Cl" ligand (Figure 3b). The high trans effect of the "═O" group is known to dramatically increase the lability of the trans "Cl" ligand. In fact, the rapid hydrolysis of the [O═Re/Tc(V)−Cl] system to [O═Re/Tc(V)−OH] was observed even in the presence of moisture.[40] Therefore, the existence of the T1 isomer of [(Me4Phen)(OH)2Re(O)Cl] in aqueous media is highly unlikely. To this end, it is reasonable to speculate that hydrolysis of **3** in aqueous media led to the formation of the T5 isomer of [(Me_4Phen)(OH)$_3$Re(O)].

Then, to further confirm the molecular composition of the hydrolyzed species in aqueous media, we isolated the hydrolyzed species by lyophilizing a solution of **3** in a DMSO/water mixture and characterized using ^{1}H and ^{13}C NMR spectroscopy, mass spectrometry, and elemental analysis. As expected, ^{1}H and ^{13}C NMR spectroscopy confirmed the absence of the EG ligand (removed during lyophilization) but the presence of the Me_4Phen ligand (Figures S11 and S12). Importantly, as noted in Table S2, elemental analysis confirmed the molecular composition of the isolated solid to be [(Me_4Phen)(OH)$_3$Re(O)]·(DMSO)$_{0.75}$. The presence of 0.75 equiv of residual DMSO was also evident in the ^{1}H and ^{13}C NMR spectra (Figures S11 and S12). Further, ESI-mass spectroscopy of a solution of the solid in MeOH showed a peak at m/z = 519.1 with the expected isotopic pattern, corresponding to the ([(Me_4Phen)(OH)$_3$Re(O)] + 2MeOH-2H_2O + H)$^+$ adduct (Figure S13). Furthermore, we compared the ^{1}H NMR spectrum of compound **3** and the isolated hydrolyzed solid of complex **3** (Figure S14). It was evident that the ^{1}H NMR signals of complex **3** in DMSO-d_6/D_2O were identical to those of the lyophilized solid of the hydrolyzed species, except for the signal from free H_2EG for complex **3**, which was removed during lyophilization of the hydrolyzed species and was absent for the isolated hydrolyzed solid. Taken together, these data firmly confirmed that complex **3** underwent hydrolysis in aqueous media through the release of both EG and Cl ligands, resulting in formation of the symmetric T5 isomer of [(Me_4Phen)(OH)$_3$Re(O)]. A similar aquation chemistry was observed for complexes **1** and **2** in aqueous media (Figures S15 and S16). Notably, the hydro-

https://doi.org/10.1021/acs.inorgchem.3c03110
Inorg. Chem. 2023, 62, 19720−19733

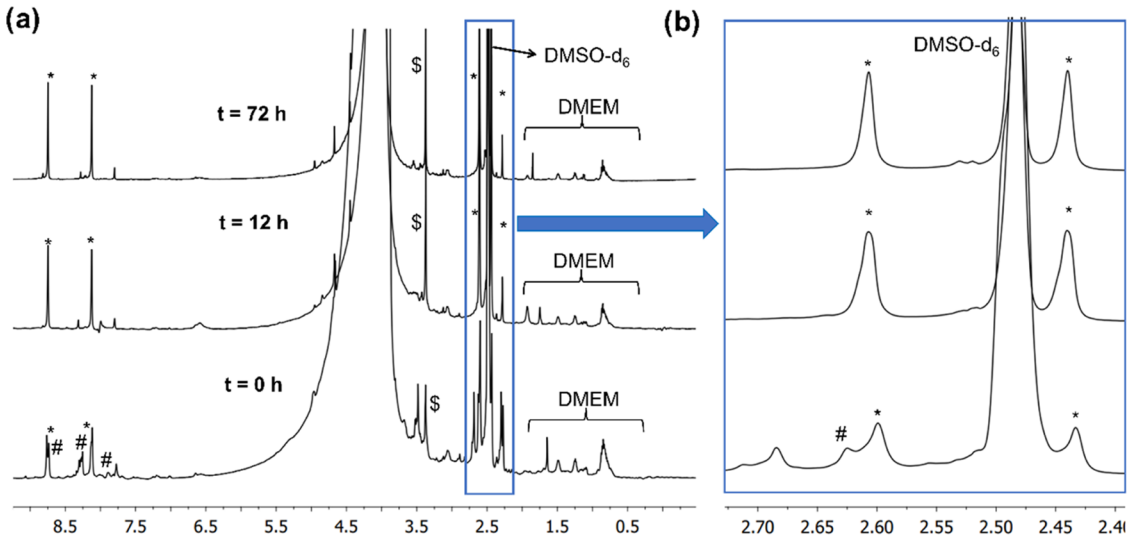

Figure 4. Stability of hydrolyzed species [$(Me_4Phen)(OH)_3Re(O)$] from complex **3** in DMEM cell culture medium. (a) Full ^{1}H NMR spectra at t = 0, 12, and 72 h and (b) zoomed aliphatic region of the same. # denotes complex **3**, * denotes the hydrolyzed species from **3**, [$(Me_4Phen)(OH)_3Re(O)$], and $ denotes free H_2EG released upon the hydrolysis of **3**.

lyzed species for **1**−**3** [$(N^\wedge N)(OH)_3Re(O)$] presented robust stability over a period of 72 h (Figures 3a, S15 and S16).

Next, we evaluated the stability of **1**−**3** in Dulbecco's modified Eagle medium (DMEM), a routinely used culture medium that contains various biological nucleophiles such as glucose, amino acids, and nucleotides, in addition to high concentrations of salts. Similar to aqueous media, complexes **1**−**3** underwent hydrolysis via releasing the EG ligand (Figures 4, S17 and S18). Interestingly, in sharp contrast to the immediate release of the EG ligand in aqueous media, complexes **1**−**3** released the EG ligand at a slower rate in DMEM (∼12 h for completion). Importantly, the hydrolyzed species [$(N^\wedge N)(OH)_3Re(O)$] remained stable for more than 72 h (Figures 4, S17 and S18). With this hydrolysis behavior in mind, we prepared a stock solution of complexes **1**−**3** for biological study in 2:1 DMSO/H_2O.

Lipophilicity and Cellular Uptake. Lipophilicity is an important physicochemical property that determines the extent of passive diffusion-mediated cellular uptake as well as the potency of anticancer agents. To tune the lipophilicity of our Re(V)═O complex, the $N^\wedge N$ ligands were varied from Bpy to Phen and Me_4Phen in complexes **1**−**3**. To investigate the influence of $N^\wedge N$ ligands on lipophilicity, the octanol−water partition coefficient (P) of **1**−**3** was measured using a shake-flask method in combination with inductively coupled plasma mass spectrometry (ICP-MS). The log P values of **1**−**3** are significantly higher (0.3−1.6) than cisplatin (−2.2) and follow the expected order **1** < **2** ≪ **3** (Figure 5). Then, we measured the cellular uptake of compounds **1**−**3** and cisplatin (as a control). Human cervical HeLa cancer cells were treated with 10 μM test compounds for 6 h, and the amount of the intracellular metal was quantified using ICP-MS. As shown in Figure 5, the uptake of **3** (1329 pmole Re/mg protein) was 3−4-fold higher than those of **1** (333 pmole Re/mg protein), **2** (413 pmole Re/mg protein), and cisplatin (386 pmole Pt/mg protein). Notably, the cellular uptake trend of Re(V)═O complexes, **1** < **2** ≪ **3**, mirrors the order of their log P values.

In Vitro Antitumor Activity and Cisplatin Cross-Resistance Profile. In vitro antitumor activity of complexes **1**−**3** was first screened against human cervical cancer cell lines

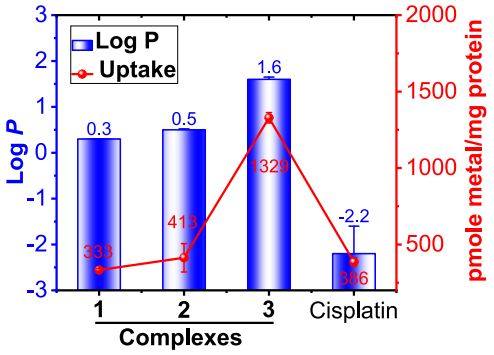

Figure 5. Log P values and cellular uptake in HeLa cells of **1**−**3** and cisplatin (10 μM, 6 h incubation). Data presented as mean ± SD of two independent experiments each performed as triplicates. The log P value of cisplatin was taken from a previously reported article.[41]

(HeLa). Free $N^\wedge N$ ligands and cisplatin were also included for comparison purposes. Cells were treated with increasing doses of the test compounds and incubated for either 24 or 72 h, and viability was evaluated using the 3-(4,5-dimethyl-2-thiazolyl)-2,5-diphenyl-2H-tetrazolium bromide (MTT) assay. Representative dose−response plots are presented in Figures S19 and S20, and half inhibitory concentrations (IC_{50}) are listed in Table 1. Complex **3** was identified to be the most potent in the series, with an $IC_{50/72h}$ value of 0.4 μM in the 72 h assay. Notably, the potency of **3** is 9-fold higher than that of cisplatin ($IC_{50/72h}$ = 3.6 μM). While complex **2** presented an $IC_{50/72h}$ value of 2.7 μM, complex **1** turned out to be inactive up to the maximum conc. tested (25 μM). A similar trend in the potency of **1**−**3** and cisplatin was observed in the 24 h incubation assays ($IC_{50/24h}$ values, Table 1). The better activity of **3** than those of **1**, **2**, and cisplatin can be attributed to its significantly higher cellular uptake (Figure 5). Interestingly, a comparison of IC_{50} values of **2** and **3** with their respective $N^\wedge N$ ligands revealed that **2** and **3** possess dramatically higher potency than their free ligands Phen and Me_4Phen, respectively. These data not only have implications in establishing the importance of the Re(V)═O core in the potency of this class of compounds but also confirm that the $N^\wedge N$ ligands remain attached to the

https://doi.org/10.1021/acs.inorgchem.3c03110
Inorg. Chem. 2023, 62, 19720−19733

Table 1. IC_{50} Values (μM) of 1−3, Bpy, Phen, Me_4Phen, Cisplatin, and Re-2 in HeLa Cells[a]

complexes	$IC_{50/24h}$ (μM); 24 h incubation	$IC_{50/72h}$ (μM); 72 h incubation
1	≥25	≥25
2	10.5 ± 0.4	2.7 ± 0.6
3	3.4 ± 0.1	0.40 ± 0.03
Bpy	≥25	≥25
Phen	≥25	13.4 ± 0.8
Me_4Phen	≥25	3.5 ± 0.1
H_2EG	≥25	≥25
cisplatin	8.2 ± 0.5	3.6 ± 0.2
[b]**Re-2**		0.69 ± 0.02

[a]Data presented as mean ± SD from three independent experiments, each performed in triplicates. [b]IC_{50} values of **Re-2** were taken for comparison purposes from ref 31.

Re(V)=O core in the active species that enter the cells. Given that the EG ligand is released from the complexes in aqueous media, we determined the cytotoxicity of free H_2EG in HeLa cells. H_2EG did not affect the cell viability up to the highest conc. tested (25 μM), suggesting a negligible contribution of the released EG ligand to the overall cytotoxicity of the Re(V)=O complexes (Table 1). Further, a comparison of the $IC_{50/72h}$ of our best complex **3** with the most potent Re(V)=O complex **Re-2** (Figure 1) reported to date suggested that complex **3** has comparable or slightly better potency than **Re-2** in HeLa cells.[31]

As mitochondrial damage and ROS induction contribute to the antitumor activity of complex **3** (discussed later), we redetermined the IC_{50} values **3** in HeLa cells using a nonenzymatic crystal violet assay. It is worth noting that the MTT assay measures the mitochondrial dehydrogenase activity and may provide unreliable IC_{50} values for mitochondria-targeted antitumor agents.[42] A crystal violet assay, on the other hand, does not rely on any enzymatic activity and rather reports the IC_{50} value based on the biomass of the adherent cells.[42] As presented in Table S3, we found that the IC_{50} values of **3** obtained from the crystal violet assay were comparable to those from the MTT assay for both 24 and 72 h (Figure S21 for dose−response plots).

Cisplatin and carboplatin are considered to be the workhorses for the management of different types of cancers in the clinic. However, inherent and acquired resistance increasingly reduces the effectiveness of these chemotherapeutics, leading to treatment failure.[9,43,44] Intrigued by the excellent potency of **3** against HeLa cells, we further evaluated its ability to circumvent cisplatin resistance. For this purpose, the $IC_{50/72h}$ values of **3** and cisplatin were determined in the wild-type cisplatin-sensitive and their matched cisplatin-resistant lung (A549 and A549 Cis), ovarian (A2780 and A2780 Cis) and prostate (DU145 and DU145 Cis) cancer cells. Dose−response plots are presented in Figure S22, and $IC_{50/72h}$ values are listed in Table 2. As anticipated, complex **3** exerted remarkably higher potency ($IC_{50/72}$ = 0.1−0.4 μM) than cisplatin ($IC_{50/72h}$ = 1.5−27.8 μM) against all six cancer cell lines. Further, potencies of **3** are comparable to those of **Re-2** (Figure 1) in A549 and A2780 cells but are ∼14-fold higher in DU145 cells.[31] Importantly, complex **3** was nearly equipotent in all three cisplatin-sensitive and matched cisplatin-resistant cells. In sharp contrast, cisplatin's effectiveness reduced drastically in cisplatin-resistant cells as compared

Table 2. $IC_{50/72h}$ Values (μM) of 3, Cisplatin, and Re-2 in Cisplatin-Sensitive (A549, A2780, and DU145) and their Matched Cisplatin-Resistant (A549 Cis, A2780 Cis, and DU145 Cis) Cells[a]

cell lines	complex 3	cisplatin	Re-2
A549	0.1 ± 0.08	1.5 ± 0.1	0.2 ± 0.01
A549 Cis	0.4 ± 0.03	27.8 ± 0.5	
RF (A549)	**4**	**18**	
A2780	0.3 ± 0.03	1.6 ± 0.6	0.2 ± 0.01
A2780 Cis	0.2 ± 0.01	12 ± 2.5	
RF (A2780)	**0.7**	**7**	
DU145	0.1 ± 0.01	1.7 ± 0.9	1.4 ± 0.08
DU145 Cis	0.1 ± 0.01	3.1 ± 1.3	
RF (DU145)	**1**	**2**	

[a]Data presented as mean ± SD from three independent experiments, each performed in triplicates. Resistance factor (RF) = $IC_{50/72h}$ value in cisplatin-resistant cells/$IC_{50/72h}$ value in matched cisplatin-resistant cells. $IC_{50/72h}$ **Re-2** was taken from for comparison purposes from ref 31.

to their matched cisplatin-sensitive cells. For better comparison purposes, we calculated the resistance factor (RF) as the ratio of $IC_{50/72h}$ values in cisplatin-resistant cells and matched cisplatin-sensitive cells. While the RF values determined for complex **3** were 4 in A549, 0.7 in A2780, and 1 for DU145, the RF determined for cisplatin were 18 in A549, 7 in A2780, and 2 for DU145 cells (Table 2). The significantly lower RF values presented by complex **3** as compared to cisplatin in any given matched pair of cell lines clearly demonstrated the ability of complex **3** to overcome cisplatin resistance in cancer cells.

To assess the cancer cell selectivity, we performed cytotoxicity evaluation of the best candidate **3** and cisplatin as control using the MTT assay on CCD18Co noncancerous colon epithelial cells and HT29 colon cancer cells. Unfortunately, similar to cisplatin ($IC_{50/72h}$, HT29 = 3.01 μM; $IC_{50/72h}$, CCD18Co = 5.09 μM), complex **3** ($IC_{50/72h}$, HT29 = 0.4 μM; $IC_{50/72h}$, CCD18Co = 0.3 μM) also presented comparable $IC_{50/72h}$ values in cancerous and noncancerous cells, suggestive of poor cancer cell selectivity (Figure S23). Therefore, further efforts are certainly required to improve the cancer cell selectivity of this class of complexes.

Intracellular Organelle Distribution of Complex 3. Next, we investigated the mechanism of the antitumor activity of our most potent complex **3**. First, to obtain preliminary insights into the possible intracellular target, HeLa cells were treated with 10 μM **3** or cisplatin (for comparison purposes) for 24 h. Important organelles such as the nucleus, cytosol, mitochondria, and insoluble membrane were isolated (detailed in the Experimental Section), and metal content (Re for complex **3** and Pt for cisplatin) in each organelle was measured using ICP-MS. The organelle distribution profiles for **3** and cisplatin are presented in Figure 6. For cisplatin-treated cells, nearly equal distribution of Pt among mitochondria (388 pmole Pt/μg protein), nucleus (274 pmole Pt/μg protein), and membrane (325 pmole Pt/μg protein) was observed. In sharp contrast, complex **3** is predominantly localized in mitochondria (1610 pmol Re/μg protein) and membrane (2104 pmol Re/μg protein), and only a trace amount was found in the nucleus (153 pmol Re/μg protein) and cytosol (116 pmol Re/μg protein). Importantly, the mitochondrial accumulation of **3** was found to be 4-fold higher as compared to that of cisplatin, suggestive of mitochondria as one of the

https://doi.org/10.1021/acs.inorgchem.3c03110
Inorg. Chem. 2023, 62, 19720−19733

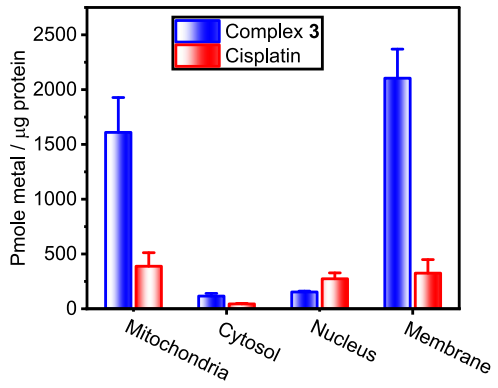

Figure 6. Intracellular organelle distribution of complex **3** and cisplatin in HeLa cells (10 μM, 24 h). Data presented as mean ± SD for two independent experiments each performed in triplicates.

prime targets for complex **3**. Further, membrane accumulation of **3** is 6.5-fold as compared to cisplatin, which can be attributed to the 3.8 log P unit higher lipophilicity of **3** as compared to cisplatin. Nevertheless, these results confirmed that complex **3** had a different intracellular distribution profile as compared to cisplatin, in addition to pointing to mitochondria and membrane as potential targets for complex **3**.

Mitochondrial Dysfunction and ROS Production. Owing to its high propensity to accumulate in mitochondria, we investigated the effect of complex **3** on mitochondria. Mitochondria are the main powerhouse and important signaling organelles for cells, which play a key role in cell survival as well as programmed cell death (PCD).[45] As altered mitochondrial dynamics and/or functioning are closely linked to the initiation, progression, and metastasis of cancer,[46,47] mitochondria are an attractive target for the development of the next generation of antitumor agents.[48] The potential of **3** to cause mitochondrial damage was assessed by measuring mitochondrial membrane potential ($\Delta\Psi_m$) in HeLa cells treated with complex **3** using the JC-1 (5,5,6,6′-tetrachloro-1,1′,3,3′-tetraethyl-imidacarbocyanine iodide) probe in combination with flow cytometry.[49,50] In healthy and functional mitochondria with intact $\Delta\Psi_m$, JC-1 forms an aggregate that emits in red. But in damaged and dysfunctional mitochondria with dissipated $\Delta\Psi_m$, JC-1 remains as a monomer that emits in green.[51] As shown in Figure 7a,7b, complex **3** treatment resulted in dramatic dose-dependent depletion of $\Delta\Psi_m$, similar to the positive control carbonyl cyanide *m*-chlorophenyl hydrazone (CCCP, Figure S24 for the dot plot).

Numerous earlier studies have demonstrated that mitochondrial damage and/or dysfunction is known to enhance intracellular oxidative stress through overproduction of reactive oxygen species (ROS).[10,52] Elevated levels of ROS cause

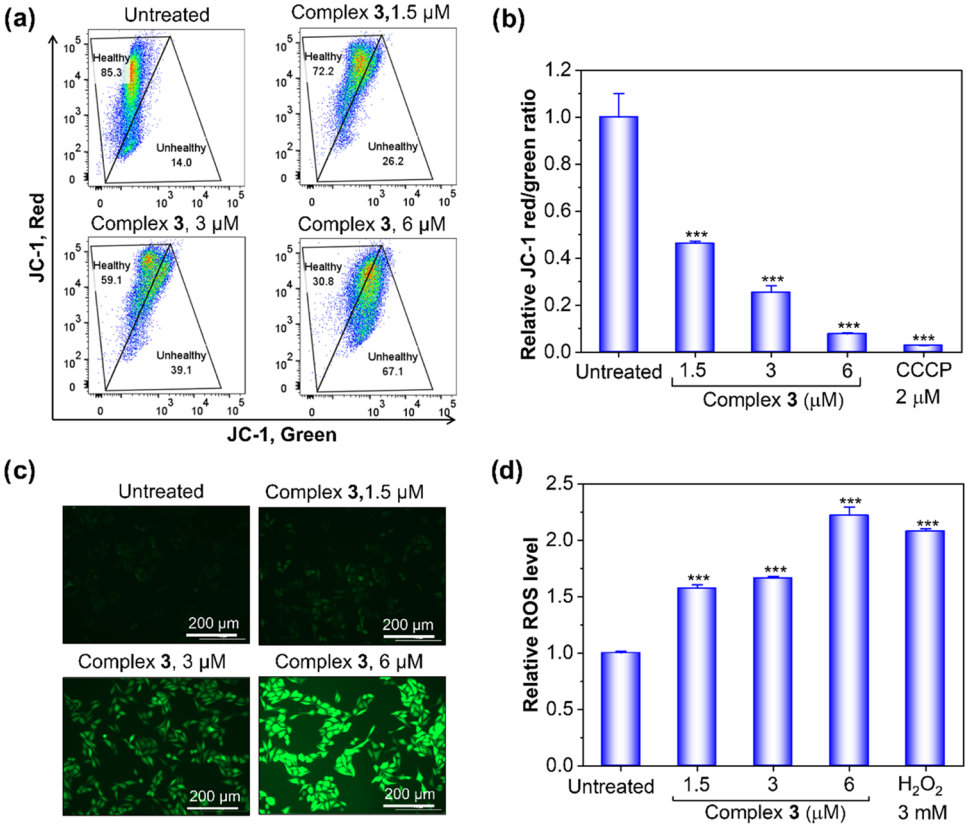

Figure 7. (a) Flow cytometry measurement of $\Delta\Psi_m$ using the JC-1 dye in HeLa cells treated with increasing concentrations of complex **3** (0−6 μM, 24 h) or CCCP (2 μM, 1 h). The dot plot for CCCP-treated cells is presented in Figure S24. (b) Quantification of relative $\Delta\Psi_m$ as the ratio of JC-1 red/JC-1 green in untreated treated cells. (c) Fluorescence microscopy images of HeLa cells stained with the DCFH-DA ROS probe after treatment with increasing concentrations of complex **3** (0−6 μM, 4 h) or H_2O_2 (3 mM, 1 h). The fluorescence microscopy image of H_2O_2-treated cells is presented in Figure S25. (d) Quantification of the relative ROS level in untreated and compound-treated cells. Note: concentrations of complex **3** were chosen to be 1.5 μM (0.5 × $IC_{50/24h}$), 3 μM ($IC_{50/24h}$), and 6 μM (2 × $IC_{50/24h}$) based on $IC_{50/24h}$ = 3.4 μM obtained from a 24 h incubation assay. Data presented as mean ± SD from two independent experiments each performed in duplicates (***p < 0.001).

https://doi.org/10.1021/acs.inorgchem.3c03110
Inorg. Chem. 2023, 62, 19720−19733

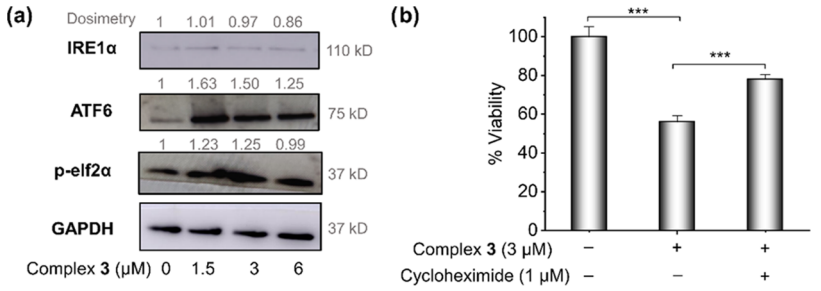

Figure 8. (a) Western blot analysis of hallmark proteins of ER stress in Hela cells treated with complex **3** (24 h exposure). The uncropped full images of all blots are presented in Figure S28. (b) Effect of cycloheximide on the viability of HeLa cells treated with complex **3**.

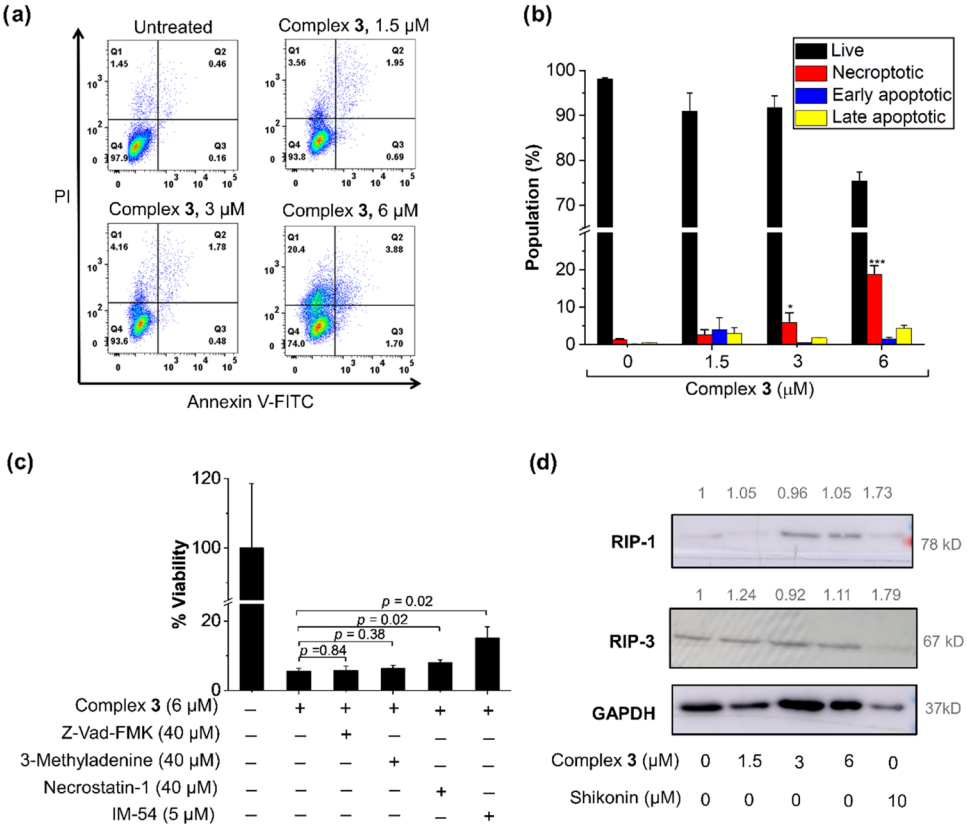

Figure 9. (a) Flow cytometry dot plots of apoptotic and necrotic population of HeLa cells left untreated or treated with 0.5 × $IC_{50/24h}$, $IC_{50/24h}$, and 2 × $IC_{50/24h}$ concentrations of complex **3** for 24 h. (b) Percent of cell population determined from dot plots. Cisplatin (a known apoptosis inducer) and H_2O_2 (a known necrosis inducer) were used for gating purposes, and corresponding dot plots are presented in Figure S27. (c) Percent viability of HeLa cells treated with 6 μM complex **3** in the absence or presence of various cell death inhibitors. Z-Vad-FMK, pan-caspase inhibitor; 3-methyladeniine, autophagy inhibitor; necrostatin-1, necroptosis inhibitor; IM-54, necrosis inhibitor. (d) Western blot analysis of necroptosis marker proteins RIP-1 and RIP-3 in HeLa cells treated with complex **3** or the known necroptosis inducer shikonin for 24 h. Images of uncropped full blots are presented in Figure S28.

oxidation of essential biomolecules and cellular reductants, leading to further enhancement of the ROS level in a vicious cyclic pathway, which impairs essential cellular processes and eventually triggers cell death. We employed a widely used ROS indicator DCFH-DA (2′,7′-dichlorodihydrofluorescein diacetate) to measure the level of ROS in cells treated with complex **3**.[41] As presented in Figure 7c,7d, HeLa cells treated with complex **3** for 4 h presented dose-dependent upregulation of intracellular ROS, similar to that of positive control H_2O_2 (Figure S25). As anticipated, the level of intracellular ROS is reduced significantly in the presence of *N*-acetyl cysteine (NAC), a known quencher of ROS (Figure S26).[53] Taken together, these data suggested that complex **3** exerts antitumor activity through mitochondrial damage-mediated induction of oxidative stress, which is consistent with the mechanism of action of Re(V)═O antitumor complex **Re-2** reported previously.[31]

ER Stress Induction. Since complex **3** caused mitochondrial damage and elevated intracellular ROS, we investigated the effect of complex **3** on the endoplasmic reticulum (ER). ER is an important organelle responsible for various essential cellular functions such as protein synthesis, folding, and transport, in addition to playing a key role in various signaling processes.[54] ER and mitochondria are closely spaced organelles that form multiple contact points through cholesterol-rich microdomains termed mitochondria-associated ER membranes

https://doi.org/10.1021/acs.inorgchem.3c03110
Inorg. Chem. 2023, 62, 19720−19733

(MAMs).[55] MAMs-mediated cross-talk between ER and mitochondria is crucial for the proper functioning of both organelles. Therefore, mitochondrial damage, $\Delta\Psi_m$ depletion, and ROS overproduction are expected to interfere with ER functioning and escalate ER stress.[17] ER stress-related signaling is transduced through three main ER transmembrane proteins—IRE1α, ATF6, and PERK. Our western blot analysis confirmed that treatment with complex **3** led to significant upregulation of ATF6 and *p*-eIF2α (a downstream protein of PERK wing) but not IRE1α (Figure 8a). Further, to investigate whether ER stress contributes to the antitumor activity of complex **3**, we studied the effect of the ER stress inhibitor cycloheximide on the potency of complex **3**. In fact, we observed an ∼22% increase in cell viability in the presence of cycloheximide as compared to cells treated with complex **3** alone (Figure 8b). Cumulatively, our mechanistic data suggested that antitumor activity of **3** involves mitochondrial damage, ROS production, and ER stress.

Characterization of the Cell Death Mechanism. Thereafter, we turned our attention to obtaining preliminary insights into the mechanism of cell death triggered by complex **3**. In general, oxidative stress, mitochondrial dysfunction, and ER stress induce apoptosis, necrosis (or necroptosis), and autophagy-mediated cell death.[17,56] Except necrosis, all other types of above-mentioned cell death are programmed cell death. First, we performed flow cytometry analysis of dual Annexin V−FITC (AV) and propidium iodide (PI) stained HeLa cells either left untreated or treated with increasing concentrations of complex **3**. Cisplatin and H_2O_2 were included as controls for gating purposes. While PI stains the nucleus of necrotic cells with compromised plasma membranes, AV binds to apoptotic cells with phosphatidyl serine flipped outside of the plasma membrane.[57] As shown in Figures 9a,b and S27, similar to the positive control H_2O_2, treatment of **3** caused a dose-dependent increase in AV^-/PI^+ necrotic population (1.4% in untreated vs 4 and 20% in 3 and 6 μM **3**-treated, respectively). No significant increase in the population of AV^+/PI^- early apoptotic and AV^+/PI^+ late apoptosis populations was observed. These data indicated that not apoptosis but necrosis was one of the main mechanisms of cell death induced by complex **3**. In line with our expectation, the pan-caspase inhibitor Z-Vad-FMK failed to inhibit the viability reduction caused by complex **3** (Figure 9c), confirming the absence of apoptosis. Necrosis has long been viewed as an accidental and unprogrammed cell death without the involvement of any molecular regulators. However, growing evidence in the recent past firmly established that necrosis may also happen in a regulated fashion mediated through RIP-1 and/or RIP-3 kinases.[31,56] The regulated form of necrosis is termed necroptosis. In order to investigate whether complex **3** elicited necrosis or necroptosis, we performed western blot analysis to check the level of RIP-1 and RIP-3 proteins in HeLa cells treated with complex **3**. As shown in Figure 9d, complex **3** treatment did not result in significant upregulation of either RIP-1 or RIP-3, while the known necroptosis inducer shikonin significantly upregulated both marker proteins. Further, the RIP-1 inhibitor necrostatin-1 had a negligible effect on the potency of complex **3**, but necrosis inhibitor IM-54 significantly reduced the potency of complex **3** by ∼2.7 fold (Figure 9c). Further, 3-methyl adenine has no effect on the potency of complex **3**, indicating the absence of autophagic cell death. Cumulatively, these data confirmed necrosis to be the major cell death mechanism evoked by complex **3**.

CONCLUSIONS

This work reports the synthesis, characterization, aquation chemistry, in vitro antitumor activity, and mechanism of action of a structurally new class of Re(V)−oxo complexes **1**−**3** of the type [(N^N)(EG)Re(O)Cl]. In aqueous media, the complexes underwent rapid hydrolysis through replacement of the EG O^O and Cl ligands with water. The resulting hydrolyzed species $[(N^N)(OH)_3Re(O)]$ presented robust stability in cell culture media DMEM over 72 h and was the active species involved in executing the cancer cell death. Owing to its highest lipophilicity, the cellular uptake efficiency of **3** is the highest among all. Concomitantly, complex **3** was identified to be the most potent in the series with $IC_{50/72h}$ values ranging from 0.1 to 0.4 μM against a panel of cisplatin-sensitive as well as cisplatin-resistant cancer cells. Notably, complex **3** presented 5−17-fold higher potency in cisplatin-sensitive HeLa, A549, A2780, and DU145 cells and 31−70-fold higher potency in cisplatin-resistant A549 Cis, A2780 Cis, and DU145 Cis cells as compared to the gold standard clinical drug cisplatin. Importantly, complex **3** was found to overcome cisplatin resistance, which is considered to be one of the major issues in managing cancers with Pt drugs in the clinic. An intracellular organelle localization study revealed that unlike cisplatin that was equally distributed among the nucleus, mitochondria, and membrane, complex **3** mainly accumulated in mitochondria and membrane. Furthermore, we demonstrated that complex **3** caused mitochondrial damage through depletion of $\Delta\Psi_m$ and upregulation of oxidative stress via production of ROS, in addition to triggering ER stress. This multipronged mechanism of action induced necrosis-mediated cell death.

EXPERIMENTAL SECTION

Materials and Methods. All chemicals and solvents used were reagent grade or better quality and were purchased from commercial suppliers. Solvents were used as received or dried with molecular sieves. All synthetic procedures were performed using standard Schlenk techniques.

Purities of newly synthesized complexes **1**−**3** used for the biological study were ≥95%, confirmed using elemental microanalysis.

NMR spectroscopic measurements were done using Bruker 800 MHz and Varian 600 MHz spectrometers at 25 °C in the NMR facility, TIFR Mumbai. All of the measurements were carried out using deuterated solvents; chemical shifts δ were reported in ppm (parts per million). The residual solvent peaks were used as an internal reference for ^1H and ^{13}C NMR spectra, and chemical shifts were expressed relative to tetramethylsilane ($SiMe_4$, δ = 0 ppm). Abbreviations for the peak multiplicities were as follows: s (singlet), d (doublet), dd (doublet of doublets), t (triplet), q (quartet), m (multiplet), and br (broad). Mass spectra were recorded on a Bruker ultrafleXtreme MALDI-TOF mass spectrometer or Thermo Q Exactive orbitrap mass spectrometer equipped with an electrospray ionization source. Simulated mass spectra were obtained from SISweb (https://www.sisweb.com/mstools.htm). Elemental microanalyses were performed on a Thermo Fisher FLASH2000 CHNS/O analyzer. Inductively coupled mass spectrometry (ICP-MS) measurements were carried out using an Agilent 7900 ICP-MS. All of the colorimetric and imaging assays were performed using a Biotec Cytation 5 Imager. Flow cytometry measurements were done using a BD FACS Aria Fusion instrument. We analyzed the immunoblots using an Amersham Imager 6000.

Synthesis and Characterization Data of Re(V)═O Complexes. *[(Bipy)(EG)Re(O)Cl] (**1**).*[38] $[(Bu)_4N][ReOCl_4]$ (62 mg, 0.1 mmol) was dissolved in 1.5 mL of MeOH, followed by addition of 0.5

https://doi.org/10.1021/acs.inorgchem.3c03110
Inorg. Chem. 2023, 62, 19720−19733

mL of ethylene glycol, and stirred at 750 rpm for 5 min at room temperature. The color of the solution changed from green to reddish brown. Bipyridine (33 mg, 0.4 mmol) was then added to the solution and stirred at 750 rpm for 30 min. The mixture was centrifuged to isolate the solid precipitate. It was then dissolved in 2 mL of $CHCl_3$ and reprecipitated using diethyl ether. The precipitate was isolated by using centrifugation and dried in high vacuum to afford complex **1** as a red-brown solid. Yield = 76% (34 mg). ^{1}H NMR ($CDCl_3$, 600 MHz): δ (ppm) = 9.32 (d, J = 5.8 Hz, 1H), 8.58 (d, J = 5.5 Hz, 1H), 8.33 (d, J = 8.1 Hz, 1H), 8.00 (d, J = 8.1 Hz, 1H), 7.90 (t, J = 7.8 Hz, 1H), 7.60 (t, J = 6.7 Hz, 1H), 7.34 (t, J = 7.8 Hz, 1H), 7.27 (d, J = 6.7 Hz, 1H), 5.57 (dd, J = 10.7, 5.6 Hz, 1H), 4.98 (td, J = 10.4, 5.2 Hz, 1H), 4.75−4.69 (m, 1H), 4.25 (dt, J = 15.4, 7.8 Hz, 1H). ^{13}C {^{1}H} NMR ($CDCl_3$, 200 MHz): δ (ppm) = 154.2, 151.9, 148.3, 142.2, 139.1, 125.7, 124.4, 123.20, 122.2, 120.1, 88.1, 87.6. MALDI-TOF: 419.1 $[\mathbf{1} - Cl]^+$, 391.1 $[\mathbf{1} - Cl - C_2H_2]^+$. Anal. calcd For **1**, $C_{12}H_{12}ClN_2O_3Re$: C, 31.75; H, 2.66; N, 6.17; found: C, 31.97; H, 3.07; N, 6.18.

*[(Phen)(EG)Re(O)Cl] (**2**).* Complex **2** was synthesized following a similar procedure as described for complex **1**, except that Phen was used, instead of Bpy, as the N^N ligand. The reaction was performed on the same scale. Complex **2** was isolated as a brown solid. Yield = 68% (32 mg). ^{1}H NMR ($CDCl_3$, 600 MHz): δ (ppm) = 9.41 (d, J = 5.4 Hz, 1H), 8.89 (d, J = 5.2 Hz, 1H), 8.38 (d, J = 8.1 Hz, 1H), 8.04 (d, J = 8.9 Hz, 1H), 8.00−7.95 (m, 1H), 7.88 (d, J = 8.9 Hz, 1H), 7.71 (d, J = 8.0 Hz, 1H), 7.66−7.59 (m, 1H), 5.72−5.61 (m, 1H), 5.12 (td, J = 10.3, 5.4 Hz, 1H), 4.74−4.64 (m, 1H), 4.29 (dd, J = 15.5, 9.9 Hz, 1H). ^{13}C{^{1}H} NMR ($CDCl_3$, 200 MHz): δ (ppm) = 141.2, 137.2, 130.4, 128.1, 128.1, 126.0, 124.7, 121.8, 88.5, MALDI-TOF: 478.3 $[\mathbf{2} + H]^+$, 443.5 $[\mathbf{2} - Cl]^+$. Anal. calcd for **2**·(diethyl ether)$_{0.2}$, $C_{14}H_{12}ClN_2O_3Re\cdot(C_4H_{10}O)_{0.2}$: C, 36.08; H, 2.86; N, 5.69; found: C, 35.94; H, 2.60; N, 5.97.

*[(Me$_4$Phen)(EG)Re(O)Cl] (**3**).* Complex **3** was synthesized following a similar procedure as described for complex **1**, except that 1 equiv of Me_4Phen was used, instead of 4 equiv of Bpy, as the N^N ligand. The reaction was performed on the same scale. Complex **3** was isolated as a brown solid. Yield = 56% (30 mg). ^{1}H NMR ($CDCl_3$, 600 MHz): δ (ppm) 9.22 (s, 1H), 8.60 (s, 1H), 8.13 (d, J = 9.4 Hz, 1H), 8.00 (d, J = 9.5 Hz, 1H), 5.62 (dd, J = 10.9, 5.5 Hz, 1H), 5.07 (td, J = 10.5, 5.3 Hz, 1H), 4.65 (dd, J = 9.6, 5.2 Hz, 1H), 4.29−4.22 (m, 1H), 3.51 (s, 3H), 2.73 (s, 3H), 2.56 (s, 3H), 2.41 (s, 3H). ^{13}C {^{1}H} NMR ($CDCl_3$, 200 MHz): δ (ppm) = 151.6, 149.9, 148.2, 141.1, 137.4, 132.9, 130.8, 128.8, 126.5, 124.0, 122.2. MALDI-TOF: 499.1 $[\mathbf{3} - Cl]^+$, 472.1 $[\mathbf{3} - C_2H_2 - Cl]^+$. Anal. calcd for **3**, $C_{18}H_{20}ClN_2O_3Re$: C, 40.48; H, 3.78; N, 5.25; found: C, 40.26; H, 3.80; N, 5.03.

DFT Calculations. All of the computations were performed using ORCA 5.0.0.[58] Geometry optimization for both Re(V) isomers, **3A** and **3B**, was carried out using the DFT B3LYP exchange−correlation functional along with dispersion correction D3 (with Becke−Johnson (BJ) damping scheme).[59−64] The basis set def2-TZVP was used for all atoms.[65] 60 core electrons of Re were replaced by def2-ECP.[66] Energy and gradient convergence criteria were set to their default values as provided in the software. For geometry optimization, tolerance values for the convergence of the energy and the root-mean-square gradient were 5×10^{-6} au and 1×10^{-4} au, respectively. For the ^{1}H NMR spectra, shielding constants for both isomers were computed using the same level of theory and basis sets. To obtain the NMR chemical shifts, we subtract the absolute shielding constant of protons in the Re(V) isomers from that of reference tetramethylsilane (TMS) protons (also computed using the same level of theory).

Aquation Chemistry. Approximately 1 mg of complexes **1**−**3** were dissolved in a mixture of 400 μL of DMSO-d_6 and 200 μL of D_2O, and ^{1}H NMR spectra were recorded at different time points up to 72 h at room temperature. The ^{1}H NMR spectra of N^N ligands and EG were also measured using identical experimental conditions.

Isolation and Characterization of the Hydrolyzed Species of Complex 3. Complex **3** (10 mg, 0.02 mmol) was dissolved in 2 mL of DMSO, and 10 mL of water was added. The mixture was lyophilized in order to obtain a pink solid. Yield = 92% (8.8 mg). ^{1}H NMR (acetone-d_6, 600 MHz): δ (ppm) = 9.18 ppm (s, 2H), 8.56 ppm (s, 2H), 2.98 ppm (s, 6H), 2.75 ppm (s, 6H). ^{13}C {^{1}H} NMR (acetone-d_6, 200 MHz): δ (ppm) = 150.2, 147.6, 136.5, 134.7, 128.0, 123.7, 16.8, 14.7. ESI-mass (in MeOH): 519.1 $[\mathbf{M} + 2MeOH - H_2O - OH]^{\cdot+}$ Elemental analysis: Anal. calcd for $[(Me_4Phen)(OH)_3Re(O)]\cdot(DMSO)_{0.75}$, $C_{17.5}H_{23.5}N_2O_{4.75}ReS_{0.75}$: C, 38.35; H, 4.32; N, 5.11; found: C, 38.12; H, 4.20; N, 5.15.

Stability of Complexes in DMEM Cell Culture Medium. Phenol-free DMEM (1 mL) was lyophilized in order to obtain powdered DMEM. The powder was dissolved in 1 mL of D_2O. Complexes **1**−**3** (∼1−2 mg) were dissolved in a mixture of 400 μL of DMSO-d_6 and 200 μL of DMEM in D_2O. Then, ^{1}H NMR spectra were recorded at different time points until 72 h.

Log *P* Measurement. A freshly prepared stock solution of complexes **1**−**3** in DMSO/H_2O (2:1) was added to 600 μL of water. A 100 uL of this solution was taken out and diluted to 5 mL using double deionized water, and the amount of Re was quantified using ICP-MS. To the 500 μL of the remaining aqueous solution, 500 μL of octanol was added. The biphasic mixture was shaken for 2 h using an orbital shaker. The mixture was then allowed to settle down for effective phase separation, and the aqueous and organic layers were carefully separated. 100 μL of the aqueous layer was carefully taken out and diluted to 5 mL using double deionized water for quantification of Re using ICP-MS. Log P was then calculated by the following formula

$$\log P = \log((C_0 - C_2)/C_2)$$

where C_0 = initial concentration of Re in ppb (preshaking) and C_2 = concentration of the metal in ppb after 2 h (postshaking).

Whole Cell Uptake. HeLa cells (2×10^6) were seeded in 60 mm Petri dishes (four Petri dishes for each complex). After 16 h, the cells were incubated with 3 mL of fresh media containing 10 μM of test complexes. All stock solutions were freshly prepared (cisplatin in PBS and complexes **1**−**3** in 2:1 DMSO/H_2O). After 6 h incubation at 37 °C, the media was aspirated, and the cells were washed with PBS (3 × 3 mL). For each complex, three Petri dishes were digested by treatment with ICP-MS grade HNO_3 (400 μL per Petri dish) for 2 days at room temperature, followed by digestion with ICP-MS grade H_2O_2 (400 μL per Petri dish) for 1 day at room temperature. The volume of each sample was made to 10 mL by adding the required amount of double deionized water. The metal content in the digested samples was measured using ICP-MS. The remaining one Petri dish was treated with RIPA buffer (200 μL for 15 min incubation at 0 °C), and then the Petri dish was scratched using a cell scraper, and the lysate was collected. The lysates were ultrasonicated in order to dissolve the membrane proteins and then ultracentrifuged at 12,000 rpm, 4 °C for 15 min, and the supernatant was collected. It was then used for measuring the total protein content using a BCA assay kit (Thermo Fisher) following the supplier protocol. The metal content in each sample was then normalized to the total protein content of the respective sample.

Cytotoxicity Assay. The cytotoxicity of compounds was evaluated using colorimetric MTT and nonenzymatic crystal violet assays. Cells (3×10^3/well for 72 h assay and 8×10^3/well for 24 h assay, 100 μL of media) were seeded in a 96-well plate and allowed to attach overnight. The following day, freshly prepared stock solutions of test complexes (cisplatin in PBS and complexes **1**−**3** in 2:1 DMSO/H_2O) were serially diluted using complete media, 100 μL was added to each well, and the cells were incubated for the desired period (24 or 72 h). The final concentration of DMSO in each well was ≤0.5%, which did not significantly affect the viability of the cell lines used. Then, the media were aspirated from all of the wells, fresh media containing (0.5 mg/mL) MTT were added, and the cells were incubated for 3 h. The media containing MTT were removed, 150 μL of DMSO was added to lyse the cells and dissolve the purple formazan crystals, and absorbance was measured at 570 nm. For the crystal violet assay, the cells were fixed with 4% PFA and treated with 0.1% Triton X in order to perforate the cells, followed by washing with PBS. Then, the cells were treated with a 0.04% crystal violet solution in PBS. The crystal violet solution was aspirated from the wells, 200 μL of ethanol was added to lyse the cells and dissolve the

https://doi.org/10.1021/acs.inorgchem.3c03110
Inorg. Chem. 2023, 62, 19720−19733

crystal violet precipitate, and absorbance was measured at 570 nm. The absorbance values were normalized to the untreated control wells and plotted against the concentration. The IC_{50} values were obtained from the resulting dose−response curves. The reported IC_{50} values were the average of two or more independent experiments, each of which had three or six replicates.

Intracellular Distribution. HeLa cells (2×10^7) were seeded in 100 mm Petri dishes (three Petri dishes per compound). The following day, the cells were incubated with 10 μM **3** or cisplatin. All stock solutions were freshly prepared (cisplatin in PBS and complexes **1**−**3** in 2:1 DMSO/H_2O). After 24 h, the media containing compounds was aspirated and washed with PBS. The cells were trypsinized and counted. The nucleus, cytoplasm, and insoluble membrane fractions were separated using the NEPER kit following the manufacturer's protocol (Thermo Fisher Scientific, #78835). The mitochondria, cytosol, and insoluble protein fractions were separated using a Mito kit following the manufacturer's protocol (Thermo Fisher Scientific, #89874). After the separation, 100 μL of RIPA was added to the insoluble fraction. The lysates were ultrasonicated in order to dissolve the insoluble proteins, if any, and then ultracentrifuged at 12,000 rpm and 4 °C for 15 min, and the supernatant was collected. Then, the protein content of each fraction was measured using the BCA assay. Then, the remaining lyases were digested using HNO_3 and H_2O_2 as described above, and the volume of each sample was adjusted to 10 mL by adding the required double deionized water. The metal content in the digested samples was measured using ICP-MS. The metal content in different samples was then normalized to the total protein content of the samples.

Measurement of Mitochondrial Membrane Potential Using the JC-1 Assay. HeLa cells (0.75×10^6) were seeded in 35 mm Petri dishes. The following day, media aspirated, and fresh medium without or with **3** (1.5, 3, or 6 μM) were added and incubated for 24 h. CCCP (2 mM, 1 h exposure) was used as a positive control. All stock solutions were freshly prepared (CCCP in DMSO and complexes **1**−**3** in 2:1 DMSO/H_2O). The cells were harvested by trypsinization, pelleted using an ultracentrifuge (1100 rpm, 5 min, 4 C), and washed with PBS (2×100 μL). Then, the cells were resuspended in 50 μL of FBS-free media containing 10 μM of the JC-1 dye and incubated for 30 min at 37 C, protected from light. The cells were again pelleted by ultracentrifugation (1100 rpm, 5 min, 4 C) and washed with PBS ($2 \times$ 100 μL). Then, the cell pellet was resuspended in 100 μL of PBS, and the fluorescence was measured using flow cytometry immediately.

Measurement of Intracellular ROS. HeLa cells (0.3×10^6) were seeded in 35 mm Petri dishes. The following day, media was replaced with fresh media without or with freshly prepared stock solution (in 2:1 DMSO/H_2O) of test compound **3** (1.5, 3 or 6 μM) or with a mixture of **3** (3 μM) and *N*-acetyl cysteine (NAC, 500 μM) and incubated for 4 h. H_2O_2 (3 mM) was used as the positive control and incubated for 1 h. The media was then removed, and the cells were incubated with FBS-free media containing DCFH-DA (10 μM) for 20 min. The media was then aspirated, the cells were washed with PBS, phenol red-free complete DMEM was added, and imaging was performed immediately. The intracellular DCF fluorescence was imaged in the GFP channel using a Cytation 5 imager using identical parameters for all Petri dishes. The experiments were performed in duplicates. We then quantified the normalized ROS by normalizing the mean GFP fluorescence with a number of cells and plotted it as a bar plot.

Annexin V/Propidium Iodide Assay. HeLa cells (0.75×10^6) were seeded in 35 mm Petri dishes. The following day, media was replaced with fresh media without or with freshly prepared stock solution (in PBS for cisplatin and in 2:1 DMSO/H_2O for **3**) of test compound **3** (1.5, 3, or 6 μM) and cisplatin (10 μM) incubated for 24 h, and H_2O_2 (3 mM) was incubated for 4 h. The cells were harvested by trypsinization and pelleted by centrifugation (1100 rpm, 5 min, 4 °C). The cell pellet was resuspended and washed with PBS (2×100 μL). Then, the cells were suspended in FBS-free media containing 10 μM Annexin V−FITC conjugate (Thermo Fisher) and 10 μM propidium iodide dye and incubated for 30 min at 37 °C, protected from light. The cells were again pelleted by centrifugation (1100 rpm, 5 min, 4 °C) and washed with PBS (2×100 μL). The cell pellets were then resuspended in 100 μL of PBS and analyzed immediately using flow cytometry.

Immunoblotting Analysis. HeLa cells (3×10^6 cells/well) were seeded in a 60 mm Petri dish. The following day, the cells were incubated with fresh media without or with **3** (1.5, 3, 6 μM) or with shikonin (10 μM) for 24 h at 37 °C. Then, the media were aspirated, the cells were washed with PBS, and RIPA buffer was added (200 μL/Petri dish, 15 min incubation at 0 °C). Then, the Petri dishes were scratched using a cell scraper to facilitate the lysis, and the protein content of the lysates was measured using a BCA assay. The lysates were then mixed with SDS-PAGE loading buffer (64 mM Tris−HCl (pH 6.8), 9.6% glycerol, 2% SDS, 5% β-mercaptoethanol, 0.01% bromophenol blue). The mixed lysates were incubated at 95 °C for 10 min and then cooled to room temperature. The lysates were loaded on 12% sodium dodecyl sulfate polyacrylamide gel such that each well contained 30 μg of the protein and resolved by electrophoresis (SDS-PAGE; 130 V for 100 min), followed by electro-transfer to the poly(vinylidene difluoride) membrane (300 mA for 1 h). Membranes were blocked in 2% (w/v) nonfat milk in PBST (PBS, 0.1% Tween 20) and incubated with the suitable primary antibodies in 1% (w/v) nonfat milk in PBST overnight at 4 °C. Then, the blots were washed with PBST (2×3 mL). The product numbers of the primary antibodies from Cell Signaling Technologies were D9G8 (p-eIF2α), 14C10 (IRE1α), D4Z8 V (ATF6), D97C12 (RIP-1), E717F (RIP-3), and D16H11 (GAPDH).

After incubation with rabbit secondary antibodies (Cell Signaling Technology, product number 7074) for 1 h at room temperature, the blots were again washed with PBST (3×3 mL). The immune complexes were then detected with an ECL detection reagent (Thermo Fisher) and analyzed using an Amersham Imager 6000 instrument fitted with a chemiluminescence filter.

Viability Assay in the Presence of Cell Death Inhibitors. The viability of HeLa cells with complex **3**, in both the presence and absence of various cell death inhibitors, was assessed using the MTT assay. A total of 8×10^3 cells per well (100 μL of media) were seeded in a 96-well plate and allowed to attach overnight. On the subsequent day, a 24 μM solution of complex **3** in cell culture media was prepared from its freshly prepared stock solution in DMSO. Solutions of different cell death inhibitors, namely, Z-Vad-FMK (apoptosis inhibitor, 160 μM), necrostatin (necroptosis inhibitor, 160 μM), 3-methyl-adenine (autophagy inhibitor, 160 μM), and IM-54 (oxidative stress-induced necrosis inhibitor, 20 μM), were prepared in complete media (1.5 mL each). To 750 μL of the inhibitor solution was added 750 μL of fresh media, and to the remaining 750 μL was added a solution of complex **3**. For the control group, 750 μL of complex **3** solution was added to 750 μL of fresh media. Subsequently, 100 μL of each final solution was added to individual wells, and the cells were incubated for a desired period (24 h). The final concentration of DMSO in each well was maintained at or below 0.5%, which did not significantly impact the viability of the utilized cell lines. Following this, the media were aspirated from all of the wells, and fresh media containing 0.5 mg/mL MTT were added. The cells were then incubated for 3 h, after which the MTT-containing media were removed. To lyse cells and dissolve the purple formazan crystals, 150 μL of DMSO was added, and absorbance was measured at 570 nm. The absorbance values for samples containing complex **3**, with or without inhibitors, were normalized to the respective control wells containing media with or without inhibitors in order to obtain the percentage viability. The reported percentage viability represents the average of two independent experiments, each of which consisted of three replicates.

■ ASSOCIATED CONTENT

Supporting Information

The Supporting Information is available free of charge at https://pubs.acs.org/doi/10.1021/acs.inorgchem.3c03110.

https://doi.org/10.1021/acs.inorgchem.3c03110
Inorg. Chem. 2023, 62, 19720−19733

^{1}H and ^{13}C NMR spectra; mass spectra; aquation chemistry and stability studies; dose−response plots; and uncropped western blot images (PDF)

AUTHOR INFORMATION

Corresponding Author

Malay Patra − *Laboratory of Medicinal Chemistry and Cell Biology, Department of Chemical Sciences, Tata Institute of Fundamental Research, 400005 Mumbai, India;* orcid.org/0000-0003-3373-6762; Email: malay.patra@tifr.res.in

Authors

Shubhangi Das − *Laboratory of Medicinal Chemistry and Cell Biology, Department of Chemical Sciences, Tata Institute of Fundamental Research, 400005 Mumbai, India*

Pulkit Joshi − *Department of Chemical Sciences, Tata Institute of Fundamental Research, 400005 Mumbai, India;* orcid.org/0000-0003-2138-6662

Complete contact information is available at: https://pubs.acs.org/10.1021/acs.inorgchem.3c03110

Author Contributions

M.P. conceptualized and supervised the project. S.D. synthesized the complexes, performed all experiments, and interpreted the data. P.J. performed theoretical studies and interpreted the results. All authors contributed to the preparation and editing of the manuscript and approved the submission.

Notes

The authors declare no competing financial interest.

ACKNOWLEDGMENTS

The authors gratefully acknowledge the financial support under project no. RTI4003 from the Department of Atomic Energy (DAE) and Tata Institute of Fundamental Research (TIFR), India. M.P. thanks the Science and Engineering Research Board (SERB), India, for financial support under the project SRG/2019/002041. The authors thank Prof. Ankona Datta and Ms. Deepika Sydelle Furtado for providing access to the elemental analyzer and helping with data collection.

REFERENCES

(1) Vaidya, S. P.; Gadre, S.; Kamisetti, R. T.; Patra, M. Challenges and opportunities in the development of metal-based anticancer theranostic agents. *Biosci. Rep.* **2022**, *42*, No. BSR20212160, DOI: 10.1042/BSR20212160.

(2) Rottenberg, S.; Disler, C.; Perego, P. The rediscovery of platinum-based cancer therapy. *Nat. Rev. Cancer* **2021**, *21*, 37−50.

(3) Wheate, N. J.; Walker, S.; Craig, G. E.; Oun, R. The status of platinum anticancer drugs in the clinic and in clinical trials. *Dalton Trans.* **2010**, *39*, 8113−8127.

(4) Johnstone, T. C.; Suntharalingam, K.; Lippard, S. J. The next generation of platinum drugs: Targeted Pt(II) agents, nanoparticle delivery, and Pt(IV) prodrugs. *Chem. Rev.* **2016**, *116*, 3436−3486.

(5) Pages, B. J.; Garbutcheon-Singh, K. B.; Aldrich-Wright, J. R. Platinum Intercalators of DNA as Anticancer Agents. *Eur. J. Inorg. Chem.* **2017**, *2017*, 1613−1624.

(6) Zhou, J.; Kang, Y.; Chen, L.; Wang, H.; Liu, J.; Zeng, S.; Yu, L. The drug-resistance mechanisms of five platinum-based antitumor agents. *Front. Pharmacol.* **2020**, *11*, No. 343, DOI: 10.3389/fphar.2020.00343.

(7) Miller, R. P.; Tadagavadi, R. K.; Ramesh, G.; Reeves, W. B. Mechanisms of Cisplatin Nephrotoxicity. *Toxins* **2010**, *2*, 2490−2518.

(8) Ott, I.; Gust, R. Non platinum metal complexes as anti-cancer drugs. *Arch Pharm.* **2007**, *340*, 117−126.

(9) Konkankit, C. C.; Marker, S. C.; Knopf, K. M.; Wilson, J. J. Anticancer activity of complexes of the third row transition metals, rhenium, osmium, and iridium. *Dalton Trans.* **2018**, *47*, 9934−9974.

(10) Cao, J.-J.; Zheng, Y.; Wu, X.-W.; Tan, C.-P.; Chen, M.-H.; Wu, N.; Ji, L.-N.; Mao, Z.-W. Anticancer Cyclometalated Iridium(III) Complexes with Planar Ligands: Mitochondrial DNA Damage and Metabolism Disturbance. *J. Med. Chem.* **2019**, *62*, 3311−3322.

(11) De Palo, A.; Draca, D.; Murrali, M. G.; Zacchini, S.; Pampaloni, G.; Mijatovic, S.; Maksimovic-Ivanic, D.; Marchetti, F. A Comparative Analysis of the In Vitro Anticancer Activity of Iridium(III) {η(5)-C(5)Me(4)R} Complexes with Variable R Groups. *Int. J. Mol. Sci.* **2021**, *22*, No. 7422, DOI: 10.3390/ijms22147422.

(12) Alessio, E.; Messori, L. NAMI-A and KP1019/1339, Two Iconic Ruthenium Anticancer Drug Candidates Face-to-Face: A Case Story in Medicinal Inorganic Chemistry. *Molecules* **2019**, *24*, No. 1995, DOI: 10.3390/molecules24101995.

(13) Leonidova, A.; Gasser, G. Underestimated Potential of Organometallic Rhenium Complexes as Anticancer Agents. *ACS Chem. Biol.* **2014**, *9*, 2180−2193.

(14) Huang, Z.; Wilson, J. J. Therapeutic and Diagnostic Applications of Multimetallic Rhenium(I) Tricarbonyl Complexes. *Eur. J. Inorg. Chem.* **2021**, *2021*, 1312−1324.

(15) Knopf, K. M.; Murphy, B. L.; MacMillan, S. N.; Baskin, J. M.; Barr, M. P.; Boros, E.; Wilson, J. J. In Vitro Anticancer Activity and in Vivo Biodistribution of Rhenium(I) Tricarbonyl Aqua Complexes. *J. Am. Chem. Soc.* **2017**, *139*, 14302−14314.

(16) Konkankit, C. C.; Vaughn, B. A.; MacMillan, S. N.; Boros, E.; Wilson, J. J. Combinatorial Synthesis to Identify a Potent, Necrosis-Inducing Rhenium Anticancer Agent. *Inorg. Chem.* **2019**, *58*, 3895−3909.

(17) King, A. P.; Wilson, J. J. Endoplasmic reticulum stress: an arising target for metal-based anticancer agents. *Chem. Soc. Rev.* **2020**, *49*, 8113−8136.

(18) Konkankit, C. C.; King, A. P.; Knopf, K. M.; Southard, T. L.; Wilson, J. J. In Vivo Anticancer Activity of a Rhenium(I) Tricarbonyl Complex. *ACS Med. Chem. Lett.* **2019**, *10*, 822−827.

(19) Marker, S. C.; King, A. P.; Granja, S.; Vaughn, B.; Woods, J. J.; Boros, E.; Wilson, J. J. Exploring the In Vivo and In Vitro Anticancer Activity of Rhenium Isonitrile Complexes. *Inorg. Chem.* **2020**, *59*, 10285−10303.

(20) Delasoie, J.; Pavic, A.; Voutier, N.; Vojnovic, S.; Crochet, A.; Nikodinovic-Runic, J.; Zobi, F. Identification of novel potent and non-toxic anticancer, anti-angiogenic and antimetastatic rhenium complexes against colorectal carcinoma. *Eur. J. Med. Chem.* **2020**, *204*, No. 112583.

(21) Sovari, S. N.; Kolly, I.; Schindler, K.; Djuric, A.; Srdic-Rajic, T.; Crochet, A.; Pavic, A.; Zobi, F. Synthesis, characterization, and in vivo evaluation of the anticancer activity of a series of 5- and 6-(halomethyl)-2,2′-bipyridine rhenium tricarbonyl complexes. *Dalton Trans.* **2023**, *52*, 6934−6944, DOI: 10.1039/D2DT04041G.

(22) Simpson, P. V.; Casari, I.; Paternoster, S.; Skelton, B. W.; Falasca, M.; Massi, M. Defining the Anti-Cancer Activity of Tricarbonyl Rhenium Complexes: Induction of G2/M Cell Cycle Arrest and Blockade of Aurora-A Kinase Phosphorylation. *Chem. - Eur. J.* **2017**, *23*, 6518−6521, DOI: 10.1002/chem.201701208.

(23) Domenichini, A.; Casari, I.; Simpson, P. V.; Desai, N. M.; Chen, L.; Dustin, C.; Edmands, J. S.; van der Vliet, A.; Mohammadi, M.; Massi, M.; Falasca, M. Rhenium N-heterocyclic carbene complexes block growth of aggressive cancers by inhibiting FGFR- and SRC-mediated signalling. *J. Exp. Clin. Cancer Res.* **2020**, *39*, No. 276, DOI: 10.1186/s13046-020-01777-7.

(24) Lo, K. K.-W. Luminescent Rhenium(I) and Iridium(III) Polypyridine Complexes as Biological Probes, Imaging Reagents, and Photocytotoxic Agents. *Acc. Chem. Res.* **2015**, *48*, 2985−2995.

(25) Clède, S.; Policar, C. Metal−Carbonyl Units for Vibrational and Luminescence Imaging: Towards Multimodality. *Chem. - Eur. J.* **2015**, *21*, 942−958, DOI: 10.1002/chem.201404600.

(26) Capper, M. S.; Packman, H.; Rehkämper, M. Rhenium-Based Complexes and in Vivo Testing: A Brief History. *ChemBioChem* **2020**, *21*, 2111−2115.
(27) Shtemenko, N.; Collery, P.; Shtemenko, A. Synergistic Effect of Cisplatin and cis-Rhenium(III) Diadamantate on TumorGrowth. In *Metal Ions in Biology and Medicine*; John Libbey Eurotext: Paris, 2006; pp 374−378.
(28) Shtemenko, N. I.; Zabitskaya, E. D.; Berzenina, O. V.; Yegorova, D. E.; Shtemenko, A. V. Liposomal Forms of Rhenium Cluster Compounds: Enhancement of Biological Activity. *Chem. Biodiversity* **2008**, *5*, 1660−1667.
(29) Martínez-Lillo, J.; Mastropietro, T. F.; Lappano, R.; Madeo, A.; Alberto, M. E.; Russo, N.; Maggiolini, M.; De Munno, G. Rhenium (IV) compounds inducing apoptosis in cancer cells. *Chem. Commun.* **2011**, *47*, 5283−5285.
(30) da S Maia, P. I.; Nguyen, H. H.; Hagenbach, A.; Bergemann, S.; Gust, R.; Deflon, V. M.; Abram, U. Rhenium mixed-ligand complexes with S,N,S-tridentate thiosemicarbazone/thiosemicarbazide ligands. *Dalton Trans.* **2013**, *42*, 5111−5121, DOI: 10.1039/c3dt32950j.
(31) Suntharalingam, K.; Awuah, S. G.; Bruno, P. M.; Johnstone, T. C.; Wang, F.; Lin, W.; Zheng, Y.-R.; Page, J. E.; Hemann, M. T.; Lippard, S. J. Necroptosis-inducing rhenium(V) oxo complexes. *J. Am. Chem. Soc.* **2015**, *137*, 2967−2974.
(32) Petrović, T.; Gligorijević, N.; Belaj, F.; Aranđelović, S.; Mihajlović-Lalić, L. E.; Grgurić-Šipka, S.; Poljarević, J. Drug combination study of novel oxorhenium(V) complexes. *J. Inorg. Biochem.* **2022**, *231*, No. 111807.
(33) Nock, B.; Maina, T.; Tsortos, A.; Pelecanou, M.; Raptopoulou, C. P.; Papadopoulos, M.; Pietzsch, H.-J.; Stassinopoulou, C. I.; Terzis, A.; Spies, H.; Nounesis, G.; Chiotellis, E. Glutathione Interaction with SNS/S Mixed-Ligand Complexes of Oxorhenium(V): Kinetic Aspects and Characterization of the Products. *Inorg. Chem.* **2000**, *39*, 4433−4441.
(34) Baird, I. R.; Mosi, R.; Olsen, M.; Cameron, B. R.; Fricker, S. P.; Skerlj, R. T. '3 + 1' mixed-ligand oxorhenium(V) complexes and their inhibition of the cysteine proteases cathepsin B and cathepsin K. *Inorg. Chim. Acta* **2006**, *359*, 2736−2750.
(35) Fricker, S. P. Cysteine proteases as targets for metal-based drugs. *Metallomics* **2010**, *2*, 366−377.
(36) Karges, J.; Cohen, S. M. Rhenium(V) Complexes as Cysteine-Targeting Coordinate Covalent Warheads. *J. Med. Chem.* **2023**, *66*, 3088−3105.
(37) Vaidya, S. P.; Manikandan, M.; Chhatar, S.; Dey, S.; Patra, C.; Patra, M. A Hydrolytically Stable Oxo-Rhenium(V) Antitumor Agent for Synergistic Combination Therapy with Cisplatin: From Synthesis and Mechanistic Studies to Toxicity Assessment in Zebrafish. *Inorg. Chem. Front.* **2023**, *10*, 6711−6727, DOI: 10.1039/D3QI01653F.
(38) Pearlstein, R. M.; Davison, A. Alkene—glycol interconversion with technetium and rhenium oxo complexes. *Polyhedron* **1988**, *7*, 1981−1989.
(39) Schutte-Smith, M.; Marker, S. C.; Wilson, J. J.; Visser, H. G. Aquation and Anation Kinetics of Rhenium(I) Dicarbonyl Complexes: Relation to Cell Toxicity and Bioavailability. *Inorg. Chem.* **2020**, *59*, 15888−15897.
(40) Tisato, F.; Mazzi, U.; Bandoli, G.; Cros, G.; Darbieu, M.-H.; Coulais, Y.; Guiraud, R. Neutral oxo and nitrido complexes of technetium(V) and rhenium(V) with an unsaturated tetradentate (N2S2) ligand. Crystal structure of [N,N′-ethylenebis(thioacetylacetonylideneiminato](2−)S,S′,N,N′) nitridotechnetium(V). *J. Chem. Soc., Dalton Trans.* **1991**, 1301−1307.
(41) Gadre, S.; Manikandan, M.; Duari, P.; Chhatar, S.; Sharma, A.; Khatri, S.; Kode, J.; Barkume, M.; Kasinathan, N. K.; Nagare, M.; Patkar, M.; Ingle, A.; Kumar, M.; Kolthur-Seetharam, U.; Patra, M. A Rationally Designed Bimetallic Platinum (II)-Ferrocene Antitumor Agent Induces Non-Apoptotic Cell Death and Exerts in Vivo Efficacy. *Chem. - Eur. J.* **2022**, *28*, No. e202201259, DOI: 10.1002/chem.202201259.
(42) Manikandan, M.; Gadre, S.; Chhatar, S.; Chakraborty, G.; Ahmed, N.; Patra, C.; Patra, M. Potent Ruthenium−Ferrocene Bimetallic Antitumor Antiangiogenic Agent That Circumvents Platinum Resistance: From Synthesis and Mechanistic Studies to In Vivo Evaluation in Zebrafish. *J. Med. Chem.* **2022**, *65*, 16353−16371, DOI: 10.1021/acs.jmedchem.2c01174.
(43) Kenny, R. G.; Marmion, C. J. Toward Multi-Targeted Platinum and Ruthenium Drugs-A New Paradigm in Cancer Drug Treatment Regimens? *Chem. Rev.* **2019**, *119*, 1058−1137.
(44) Anthony, E. J.; Bolitho, E. M.; Bridgewater, H. E.; Carter, O. W. L.; Donnelly, J. M.; Imberti, C.; Lant, E. C.; Lermyte, F.; Needham, R. J.; Palau, M.; Sadler, P. J.; Shi, H.; Wang, F.-X.; Zhang, W.-Y.; Zhang, Z. Metallodrugs are unique: opportunities and challenges of discovery and development. *Chem. Sci.* **2020**, *11*, 12888−12917.
(45) Tait, S. W. G.; Green, D. R. Mitochondrial regulation of cell death. *Cold Spring Harbor Perspect. Biol.* **2013**, *5*, No. a008706, DOI: 10.1101/cshperspect.a008706.
(46) Anderson, G. R.; Wardell, S. E.; Cakir, M.; Yip, C.; Ahn, Y.-R.; Ali, M.; Yllanes, A. P.; Chao, C. A.; McDonnell, D. P.; Wood, K. C. Dysregulation of mitochondrial dynamics proteins are a targetable feature of human tumors. *Nat. Commun.* **2018**, *9*, No. 1677.
(47) Wallace, D. C. Mitochondria and cancer. *Nat. Rev. Cancer* **2012**, *12*, 685−698.
(48) Roth, K. G.; Mambetsariev, I.; Kulkarni, P.; Salgia, R. The Mitochondrion as an Emerging Therapeutic Target in Cancer. *Trends Mol. Med.* **2020**, *26*, 119−134.
(49) Pan, Z.-Y.; Tan, C.-P.; Rao, L.-S.; Zhang, H.; Zheng, Y.; Hao, L.; Ji, L.-N.; Mao, Z.-W. Recoding the cancer epigenome by intervening in metabolism and iron homeostasis with mitochondria-targeted rhenium(I) complexes. *Angew. Chem., Int. Ed.* **2020**, *59*, 18755−18762.
(50) Zhu, Z.; Wang, Z.; Zhang, C.; Wang, Y.; Zhang, H.; Gan, Z.; Guo, Z.; Wang, X. Mitochondrion-targeted platinum complexes suppressing lung cancer through multiple pathways involving energy metabolism. *Chem. Sci.* **2019**, *10*, 3089−3095.
(51) Perelman, A.; Wachtel, C.; Cohen, M.; Haupt, S.; Shapiro, H.; Tzur, A. JC-1: alternative excitation wavelengths facilitate mitochondrial membrane potential cytometry. *Cell Death Dis.* **2012**, *3*, No. e430, DOI: 10.1038/cddis.2012.171.
(52) Erxleben, A. Mitochondria-Targeting Anticancer Metal Complexes. *Curr. Med. Chem.* **2019**, *26*, 694−728.
(53) Zhitkovich, A. N-Acetylcysteine: Antioxidant, Aldehyde Scavenger, and More. *Chem. Res. Toxicol.* **2019**, *32*, 1318−1319.
(54) Phillips, M. J.; Voeltz, G. K. Structure and function of ER membrane contact sites with other organelles. *Nat. Rev. Mol. Cell Biol.* **2016**, *17*, 69−82.
(55) Zhang, Y.; Wu, Y.; Zhang, M.; Li, Z.; Liu, B.; Liu, H.; Hao, J.; Li, X. Synergistic mechanism between the endoplasmic reticulum and mitochondria and their crosstalk with other organelles. *Cell Death Discovery* **2023**, *9*, No. 51, DOI: 10.1038/s41420-023-01353-w.
(56) Tan, C.-P.; Lu, Y.-Y.; Ji, L.-N.; Mao, Z.-W. Metallomics insights into the programmed cell death induced by metal-based anticancer compounds. *Metallomics* **2014**, *6*, 978−995.
(57) Wlodkowic, D.; Skommer, J.; Darzynkiewicz, Z. Flow cytometry-based apoptosis detection. In *Apoptosis*; Springer, 2009; pp 19−32.
(58) Neese, F. The ORCA program system. *WIREs Comput. Mol. Sci.* **2012**, *2*, 73−78.
(59) Becke, A. D. Density-functional thermochemistry. III. The role of exact exchange. *J. Chem. Phys.* **1993**, *98*, 5648−5652.
(60) Lee, C.; Yang, W.; Parr, R. G. Development of the Colle-Salvetti correlation-energy formula into a functional of the electron density. *Phys. Rev. B* **1988**, *37*, 785−789.
(61) Vosko, S. H.; Wilk, L.; Nusair, M. Accurate spin-dependent electron liquid correlation energies for local spin density calculations: a critical analysis. *Can. J. Phys.* **1980**, *58*, 1200−1211.
(62) Stephens, P. J.; Devlin, F. J.; Chabalowski, C. F.; Frisch, M. J. Ab Initio Calculation of Vibrational Absorption and Circular Dichroism Spectra Using Density Functional Force Fields. *J. Phys. Chem. A* **1994**, *98*, 11623−11627.

(63) Grimme, S.; Ehrlich, S.; Goerigk, L. Effect of the damping function in dispersion corrected density functional theory. *J. Comput. Chem.* **2011**, *32*, 1456−1465.
(64) Grimme, S.; Antony, J.; Ehrlich, S.; Krieg, H. A consistent and accurate ab initio parametrization of density functional dispersion correction (DFT-D) for the 94 elements H-Pu. *J. Chem. Phys.* **2010**, *132*, No. 3382344.
(65) Weigend, F.; Ahlrichs, R. Balanced basis sets of split valence, triple zeta valence and quadruple zeta valence quality for H to Rn: Design and assessment of accuracy. *Phys. Chem. Chem. Phys.* **2005**, *7*, 3297−3305.
(66) Andrae, D.; Häußermann, U.; Dolg, M.; Stoll, H.; Preuß, H. Energy-adjustedab initio pseudopotentials for the second and third row transition elements. *Theor. Chim. Acta* **1990**, *77*, 123−141, DOI: 10.1007/BF01114537.

https://doi.org/10.1021/acs.inorgchem.3c03110
Inorg. Chem. 2023, 62, 19720−19733